

Exploiting Supramolecular Assemblies for Filterless Ultra-Narrowband Organic Photodetectors with Inkjet Fabrication Capability

Surendra B. Anantharaman,^{,a,b} Karen Strassel,^{a,c} Matthias Diethelm,^{a,b} Agnes Gubicza,^d
Erwin Hack,^d Roland Hany,^a Frank A. Nüesch,^{*,a,b} and Jakob Heier^a*

^a Laboratory for Functional Polymers, Empa, Swiss Federal Laboratories for Materials Science and Technology, Überlandstrasse 129, CH-8600 Dübendorf, Switzerland

^b Institut des Matériaux, École Polytechnique Fédérale de Lausanne, EPFL Station 12, CH-1015 Lausanne, Switzerland

^c Institute of Chemical Sciences and Engineering, École Polytechnique Fédérale de Lausanne, EPFL, CH-1015 Lausanne, Switzerland

^d Transport at Nanoscale Interfaces, Empa, Swiss Federal Laboratories for Materials Science and Technology, Überlandstrasse 129, CH-8600 Dübendorf, Switzerland

Keywords: supramolecular assemblies, J-aggregates, organic dyes, ultra-narrowband photodetectors, color selective, solution processability

Corresponding Authors

* [F.A.N \(frank.nuesch@empa.ch\)](mailto:Frank.Nuesch@empa.ch) or S.B.A (surendrababu87@gmail.com)

† Electronic supplementary information (ESI)

Abstract

Narrowband photodetectors are useful for myriad applications involving color discrimination as well as biological imaging and machine vision. Prevalent devices use broadband light absorbing materials in conjunction with electric (charge collection narrowing, photo multiplication) and optical strategies (optical cavity) to narrow down the spectral response of the detector. Here we exploit the intrinsic narrow absorption width of ~13-50 nm peculiar to J-aggregates of strongly coupled cyanine dye molecules for narrowband photodetectors. Albeit using ultrathin J-aggregate films (10 nm) the unparalleled optical aggregate properties lead to high external quantum efficiency (15 %) and response speed (15 kHz) at low bias voltage (-1 V). We show that the self-assembly process and device architecture used permit to incorporate J-aggregates of various cyanine dyes with photodetection maxima ranging from the visible to the near-infrared region up to 1000 nm. Narrow bandwidth (< 50 nm) photodetectors fabricated by inkjet printing the active device layers including the J-aggregate film perform on par with spin-coated devices, thus underlining their industrial potential.

1. Introduction

Today's world of telecommunication, automation and digitization is in demand of photodetectors that efficiently convert incident photons into an electrical signal. Most commercial photodetectors are based on silicon or compound semiconductors with broadband absorption covering the ultraviolet (GaN),¹ visible (Si)² and near infrared (InGaAs)³ subbands, respectively. Of great interest has been CMOS integration for imaging applications, which however is mainly restricted to silicon or requires complicated and expensive manufacturing processes.⁴ The ever increasing demand in consumer electronics, mobile devices, automobile, machine vision and security therefore asks for novel device concepts, materials and fabrication processes.⁵

Of particular interest are color sensing devices having narrowband spectral sensitivity with a full-width at half maximum (FWHM) of less than 100 nm.^{6,7} This allows for better imaging resolution and avoids interference from light with wavelengths not of interest. For instance, in biological imaging, it is important to have photodetectors with maximum selectivity in the near infrared (NIR) region (800-1450 nm) matching the transparency window of biological tissue.⁸ Narrowband photodetectors can also find promising applications in optical communications, color imaging and security surveillance.⁵

Common spectral discrimination is achieved by using broadband detectors in combination with a set of optical filters.⁹ New developments are proposed, where filtering inks can be solution deposited directly on top of photodetector devices.¹⁰ Recently, filterless strategies have been devised to limit the broadband detectors' response to a narrow range. They are based on charge collection narrowing (CCN),¹¹⁻¹³ micro-cavities for interference narrowing¹⁴ and for harvesting charge-transfer (CT) states¹⁵ as well as optical field enhancement at plasmon resonances.^{16,17} Colloidal

quantum dot (CQD) based materials such as PbS, CdSe(S) and lead-halide perovskites attract particular attention owing to their processability from solution allowing convenient integration in conventional silicon electronics.^{11,18,19} As for all inorganic semiconductors, CQDs have a broad intrinsic photosensitivity.²⁰ By applying the CCN approach, narrowband response was obtained from micro-meter thick CQD films.^{10–12} Nanowires were shown to provide narrowband photodetectors over a large spectral domain (600 nm – 1600 nm).²¹ Albeit compelling with respect to narrowband sensitivity, CCN has the drawback to increase response time and operating voltage and to decrease the external quantum efficiency (EQE) of the detector. For instance, Fang et al.¹¹ have shown ultra-narrowband single crystal perovskite films with FWHM < 20 nm. However, the EQE in these devices is less than 3% when biased at -4 V. Eventually, organic semiconductor materials are extremely interesting for narrowband photodetector devices due to the intrinsic narrowness of discrete optical π - π^* transitions of its molecular constituents.^{22,23} Furthermore, due to the low charge carrier mobility in these films, such devices are predestined for charge collection narrowing, where collection efficiency depends on the penetration depth of light into the semiconductor film.^{24,25} Nevertheless, organic photodetectors (OPD) with a narrow spectral response (FWHM < 100 nm) performing with high EQE at low voltage have yet to be realized.

Organic salts like cyanine dyes have recently been used for solar cell and photodetector applications in a wide spectral domain ranging from the ultra-violet to the near-infrared.^{26–29} The synthesis routes of cyanine dyes have benefited from many decades of research and development in the field of photography, data storage and biolabeling.^{30–32} While these dyes show a unique narrow absorption band in solution, their solid state thin film absorption is broadened as a result of intermolecular interactions.³³ Due to the very strong transition dipole moment of cyanine chromophores

and their tight packing in supramolecular assemblies, exciton coupling is particularly strong, giving rise to spectroscopic H- or J-aggregates which may dominate the absorption spectrum.³⁴ Utilizing particular self-assembly techniques, pure J-aggregates can be obtained showing extremely narrow absorption bands (FWHM < 20 nm) along with coherent exciton diffusion in tightly packed molecular assemblies.^{35–38} Such intrinsic material features are unique and highly desirable for narrowband photodetectors relying neither on filtering approaches nor on CCN. Osedach et al.³⁹ have shown that J-aggregates of cyanine dyes can be used in a NIR photodetector with peak sensitivity at 756 nm. The device architecture included an optical spacer and a thick Ag electrode to enhance reflectivity. An EQE of around 15% at 0 V bias was achieved, however, due to interference effects from the cavity, the EQE spectrum was much broader and blue-shifted with respect to the J-aggregate peak absorption of the thin film.

Organic semiconductors in general benefit from low-cost solution processability, which is an attractive feature for integration of such photodetectors in read-out integrated circuitry.⁴⁰ This is particularly relevant when the photodetector device architecture can be printed with high spatial resolution.^{41,42} Advantageously, aqueous J-aggregate inks can be produced, which are suitable for inkjet printing. Although reports on patterned inkjet printed J-aggregate films^{43,44} highlight the potential of the narrow band aggregates in printed electronics, the spectral characteristics of the printed J-aggregates have not been exploited successfully for a narrowband photodetector.

In this work, we further exploit the unique properties of J-aggregates for narrowband photodetection. The variation of the polymethine chain length allows spanning a considerable spectral region from the visible to the NIR. A trimethine, pentamethine as well as a heptamethine dye are used for the formulation of J-aggregate inks with excellent ultrathin film forming properties. The benefit of a robust

photodetector device architecture implementing oxide layers for selective charge transport and its effect on external quantum efficiency is discussed. Eventually we show that the active materials used for the fabrication are fully compatible with inkjet printing and demonstrate a printed narrowband (FWHM < 50 nm) photodetector with an EQE comparable to the spin-coated control device.

2. Experimental Section

2.1. J-aggregate formation

Three different cyanine dyes were procured from FEW Chemicals, Germany, namely - 5,6-dichloro-2-[[5,6-dichloro-1-ethyl-3-(4-sulfobutyl)-benzimidazol-2-ylidene]-propenyl]-1-ethyl-3-(4-sulfobutyl)-benzimidazolium hydroxide, inner salt, sodium salt (**J580**); 5-chloro-2-[5-[5-chloro-3-(4-sulfobutyl)-3H-benzothiazol-2-ylidene]-3-phenyl-penta-1,3-dienyl]-3-(4-sulfobutyl)-benzothiazol-3-ium hydroxide, inner salt, triethylammonium salt (**J780**); and 5-chloro-2-[2-(3-[2-[5-chloro-3-(4-sulfobutyl)-3H-benzothiazol-2-ylidene]-ethylidene]-2-phenylcyclohex-1-enyl)-vinyl]-3-(4-sulfobutyl)-benzothiazol-3-ium hydroxide, inner salt, triethylammonium salt (**J980**). The dyes were used without further purification. 0.5 wt.% of the **J580** dye was dissolved in water to form J-aggregates in solution. For **J780** and **J980**, the dye (0.5 wt.%) was dissolved in 100 mM potassium acetate buffer (pH 3.5-4) to form J-aggregates in solution. The solutions were stirred at 300 rpm overnight at room temperature before deposition. Alternatively, monomer solutions were prepared containing 0.5 wt.% dye dissolved in 2,2,2-tri-fluoroethanol (TFE).

2.2. Fabrication of narrowband photodetectors

Indium Tin Oxide (ITO) substrates (Geomatec, resistivity $\sim 11 \text{ Ohms}/\square$) were cleaned by ultrasonication in acetone, ethanol, Hellmanex, and water for 10 min separately. Titanium iso-propoxide (Sigma Aldrich) was spin-coated on cleaned ITO substrates and subsequently annealed at 460°C for 2 h to obtain a compact TiO_2 layer as reported elsewhere.⁴⁵ Annealed TiO_2 substrates were treated with oxygen plasma with a power setting of 45 W for 5 min. The J-aggregate solution was spin-coated on ITO/ TiO_2 substrates for 30 s at 4000 rpm. The thickness of TiO_2 is $\sim 35 \text{ nm}$. The J-aggregate thickness for **J580** is $\sim 20 \text{ nm}$ while for **J780**, **J980** it is $\sim 10 \text{ nm}$. The device was completed with a 50 nm thick vapor deposited 4,4'-cyclohexylidenebis[N,N-bis(4-methylphenyl)benzenamine] (TAPC, Sigma Aldrich) electron blocking layer and a 10 nm thick thermally evaporated molybdenum (VI) oxide (MoO_3 , 99.97%, Sigma Aldrich) hole extraction layer. A 12 nm thick Ag (Kurt J. Lesker) electrode was deposited through a shadow mask defining photodiodes with active areas of 3.1 and 7.1 mm^2 .

2.3. Fabrication of inkjet printed photodetectors

Preparation of inks. Titanium diisopropoxide bis(acetylacetonate) with 75 wt.% in isopropanol (Sigma Aldrich) was further diluted in isopropanol to a ratio of 1:20 to be used as ink for a compact TiO_2 (c- TiO_2) layer. The ink for a mesoporous TiO_2 (m- TiO_2) layer was prepared from a TiO_2 nanoparticle suspension (Ti-Nanoxide, Solaronix) with particle sizes $\sim 15\text{-}20 \text{ nm}$ dispersed with 18 wt.% in terpineol medium. This stock solution was further diluted in terpineol to a 1:10 ratio. J-aggregates were prepared from the **J580** dye by dissolving 5 mg of the dye in 1 ml (0.5 wt.%) of Millipore water. The solutions were ultrasonicated for 5 min before printing the J-aggregates.

2.4. Inkjet printing

ITO substrates were pre-cleaned as described above. Prior to inkjet printing, the substrates were cleaned by an oxygen plasma treatment for 5 min. The compact-TiO₂, mesoporous-TiO₂ and J-aggregates were printed using the PiXDRO LP50 Inkjet system (Meyer Burger) equipped with a Spectra printhead module (SL-128 AA, 80 picoliter, Fujifilm Dimatix Inc.). After post-printing the compact-TiO₂ and mesoporous-TiO₂ layers, the substrates were annealed at 460 °C for 2 h followed by inkjet printing J-aggregates and drying at room temperature. Subsequently, the inkjet printed half-cells were transferred into a thermal evaporator chamber to complete the devices by sequential thermal evaporation of 50 nm of TAPC, 10 nm of MoO₃ layer and 60 nm of Ag.

2.5. Characterizations. Film attenuances were measured using a Varian Cary 50 UV-vis spectrophotometer and the baseline was corrected by subtracting the attenuance of the substrate used (glass or ITO/TiO₂). The morphology of the thin films was studied using atomic force microscopy (Bruker Dimension Icon) in tapping mode. J-V characteristics of the cells were acquired by exposing the cells from the ITO side to AM 1.5 solar irradiation from a Spectra-Nova solar simulator. External quantum efficiency (EQE) of the cells was measured using a commercial setup (SpeQuest, ReRa solutions BV) by calibrating the system with a Si photodiode. The responsivity (R) was calculated from the EQE ($R = EQE \times e \times \lambda/hc$), where e is the elementary charge, h is Planck's constant and c is the speed of light.

The specific detectivity (D^*) of a photodetector is given by the following expression:

$$D^* = (A\Delta f)^{1/2} R/i_n$$

with A the area of the detector in cm^2 , R the responsivity in A/W and i_n the current noise in A integrated over the bandwidth Δf . In order to characterize the current noise of the system, the current was recorded as a function of time using a Stanford SR570 current amplifier while DC biasing the sample via the input of the amplifier. The noise power spectral density was calculated from the obtained data.⁴⁶ The noise measurements were performed under dark conditions. The current noise values were chosen at the response speed ($f_{-3\text{dB}}$) of the photodetector for calculating the noise equivalent power (NEP) and specific detectivity. The response speed of the photodetector was measured using a Paios (Fluxim AG) system by modulating the frequency of the light pulse and recording the photocurrent at different bias voltage. For impedance spectroscopy, the device was maintained at zero bias voltage while sweeping the frequency from 10 MHz to 10 Hz. The impedance was recorded at different light intensity to study the RC effect. The optical constants $n(\lambda)$ and $k(\lambda)$ as a function of wavelength (λ) were obtained by variable angle spectral ellipsometry (M-2000 VI, J.A. Woollam Co.).

3. Results and Discussion

3.1. Molecular and solvent engineering approach for J-aggregate thin films

We explored a trimethine (**J580**), a pentamethine (**J780**) and a heptamethine dye (**J980**) (Fig. 1a – c) to investigate the formation of J-aggregates in solution and thin films covering a broad range of wavelengths from the red to the NIR region. Two of these dyes are already known to form J-aggregates in solution. The **J580** dye is well-known to form J-aggregates in water^{47,48}, which is not the case for the **J780** dye that forms undesired H-aggregates in this solvent. However, upon addition of sodium chloride J-aggregation can be induced for the **J780** dye.⁴⁹ In previous work, we showed that J-aggregate formation can also be induced in acetate buffer even at low dye

concentration.^{38,50} We applied the same strategy successfully to the **J780** and **J980** dyes and obtained narrow-banded aggregates in solution. Compared to the monomer absorption obtained from methanol solution, the absorption peaks are redshifted by 100-200 nm and present significantly narrowed widths (Fig. S1, ESI†). In summary, all three dyes form J-aggregates in aqueous (buffer) solution with peak positions at 586 nm (**J580**), 780 nm (**J780**) and 980 nm (**J980**).

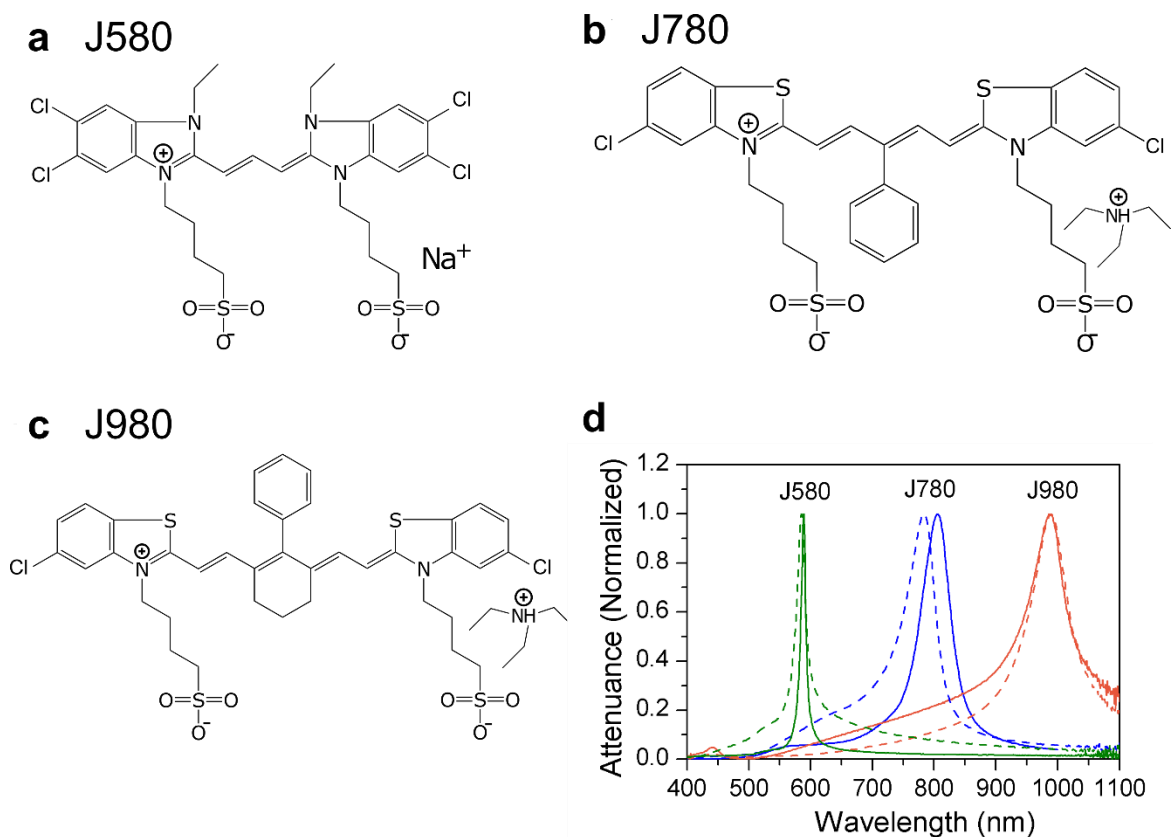


Fig. 1 Chemical structure of the (a) **J580**, (b) **J780** and (c) **J980** dye. (d) Comparison of attenuance peaks of aggregate thin films when suspended aggregates are directly deposited from solution (solid line) or obtained in-situ during spin-coating from a monomer solution (dotted line) on ITO/TiO₂ substrate.

One recurring challenge in fabricating organic thin film devices is to produce high quality thin films with low roughness and a minimum number of defects like pinholes, grain boundaries or crystal interfaces. This is particularly challenging in our case, since J-aggregates consist of two-dimensional platelets complicating the realization of a continuous surface coverage.⁴⁸ A number of methods are known which are susceptible to form homogeneous and continuous films. These approaches include nucleation of aggregates of a critical size on the substrate followed by crystalline growth fed from monomers from solution as well as layer-by-layer deposition or Langmuir Blodgett techniques, which are all time consuming.^{48,51,52}

Here we investigated two rapid growth methods, which would be more interesting from a commercial point of view. The first method (hereafter called direct method) consists of directly spin-coating the aqueous J-aggregate solutions at high rates of 4000 rpm onto the glass substrate. Albeit this method merely deposits solvated J-aggregates onto the substrate, the altered concentration and electrostatic conditions in the solid film may well induce severe changes to the molecular packing and hence to the spectral features. In previous work, we have observed such changes when depositing J-aggregates on functionalized surfaces.³⁸ Here we found, however, that J-aggregate films retained the desired optical properties such as high oscillator strength and narrow absorption width (Fig. 1d). This direct deposition method bears the disadvantage that the resulting film quality reflects the size and morphology of suspended particles in solution. In the case of the larger crystallites obtained in acetate buffer solution (**J780** and **J980**), the film morphology was poor and the film showed large crystalline domains and numerous pinholes (Fig. 2a).³⁹

Alternatively to the direct method, we coated films from cyanine monomer solutions (hereafter called in-situ method) using TFE as solvent, which has a low boiling

point but a larger dipole moment than water. The high solubility of the dyes in TFE prevents aggregation in solution, however, dye monomers were effectively transformed into J-aggregated films (Fig. S2, ESI†). Furthermore, the uniformity of films formed by this in-situ method improved significantly and the crystallite sizes and porosity between the stacked sheets was clearly reduced (Fig. 2b). The influence of the two different solvent engineering approaches on device performance will be explained below.

From an optical point of view, high-quality J-aggregates are characterized by a large redshift, narrow FWHM and the absence of vibronic shoulders in the absorption spectra. Attenuance spectra of the dye aggregates manufactured by the two different (direct and in-situ) methods are shown in Fig. 1d. For the **J580** dye, the aggregate film deposited by the in-situ route has a smaller redshift, a much broader FWHM and a pronounced shoulder compared to the J-aggregates deposited directly from solution. A similar behavior can be observed for the **J780** dye. While the aggregated film deposited directly from solution still has a larger redshift, the FWHM is the same and only a small high energy shoulder persists in the in-situ film. For the **J980** dye, aggregates formed in situ have superior optical properties compared to the aggregates formed by the direct method. In order to assess possible interference and scattering effects, we further investigated the thin J-aggregate films by variable angle spectroscopic ellipsometry. The absorption coefficients $k(\lambda)$ of the thin films (Fig. S3, ESI†) show a narrow FWHM of the J-aggregate band similar to the attenuance spectra. The film thicknesses ranged between 15 nm and 20 nm, pinpointing the ultrathin nature of these films.

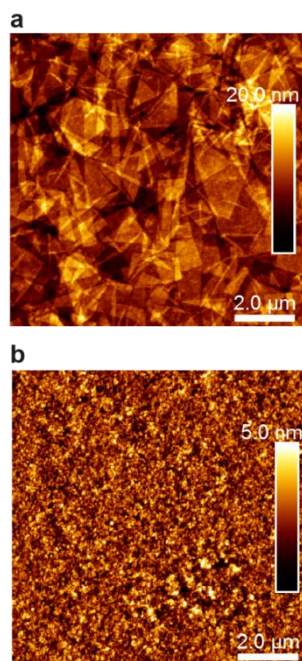


Fig. 2 Difference in film morphology of **J780** dye aggregates on ITO/ TiO_2 substrates fabricated by the (a) direct method from solution or (b) in-situ method from TFE solution.

To summarize these results, the in-situ formation of J-aggregates upon spin-coating monomers from TFE solution results in more uniform and continuous films as compared to the method where J-aggregates are deposited directly from solution. On the other hand, the optical properties show a different trend for each dye: a narrower FWHM is observed for **J580** when deposited by the direct method, while **J780** shows similar spectral width between both methods and for **J980** the in-situ method proved best.

3.2. Narrowband Photodetectors

Devices with all three dyes were fabricated following a simple structure. The photoactive J-aggregate film was sandwiched between a TiO_2 electron acceptor and a MoO_3 hole extraction layer. The entire detector was built on top of a glass-ITO electrode and completed with an Ag top-electrode (Fig. 3a, top-view for the electrode arrangement is shown in Fig. S5a, ESI†). In order to compare the effect of film deposition method on device performance, the J-aggregate

layers for **J780** and **J980** were fabricated by the in-situ as well as the direct method. Focusing on narrowband photodetectors, **J580** films were only manufactured by the direct method. To minimize the effect of shunts due to pinholes in the J-aggregate layer we also report **J580** device results where an additional TAPC electron blocking layer was introduced between the J-aggregate film and MoO₃. The energy level diagram of the devices is shown in Fig. 3b taking the **J580** data from the literature.⁵³ *J-V* curves for all devices are shown in Fig. 3c – f and in the Fig. S4-S6, ESI†. Devices with **J580** showed high rectification and considerably low dark current, but the breakdown voltage was low at -1 V (Fig. 3c). Adding TAPC as blocking layer deteriorated the diode characteristics of the device. Dark current and photocurrent decreased drastically, implying that pinholes in the rough **J580** layer could indeed be neutralized by the add-layer (Fig. 3d). The reason for the lowered photocurrent can be attributed to low hole extraction efficiency induced by the misalignment of the highest occupied molecular orbital (HOMO) energy level of the TAPC layer and the work function of MoO₃.⁵⁴ Advantageously, the J_{light}/J_{dark} ratio between the current under irradiation and in the dark measured at a bias of -1 V was higher than for **J580** devices without blocking layer, and the photodetector could be driven at a higher reverse bias of -4 V without breakdown. The **J780** devices spin-coated from TFE solution showed a better rectification behavior with reduced number of shunts, in comparison to the J-aggregates spin-coated from acetate buffer solution (Fig. 3e and Fig. S5). The **J980** devices showed improved rectification as well as a higher short circuit current density (J_{sc}) and J_{light}/J_{dark} ratio when fabricated by the in-situ method (Fig. 3f and Fig. S6, ESI†). The integrated current density (ICD) values obtained from the convolution of the EQE spectra measured at different biases and the AM1.5 solar spectrum are indicated in the *J-V* plots of Fig. 3. A marked difference between the integrated current density values from the EQE and the measured J_{sc} values can be observed for **J980** devices (Fig. 3f). This difference may stem from the overlap of the narrow J-aggregate absorption band with the sharp emission

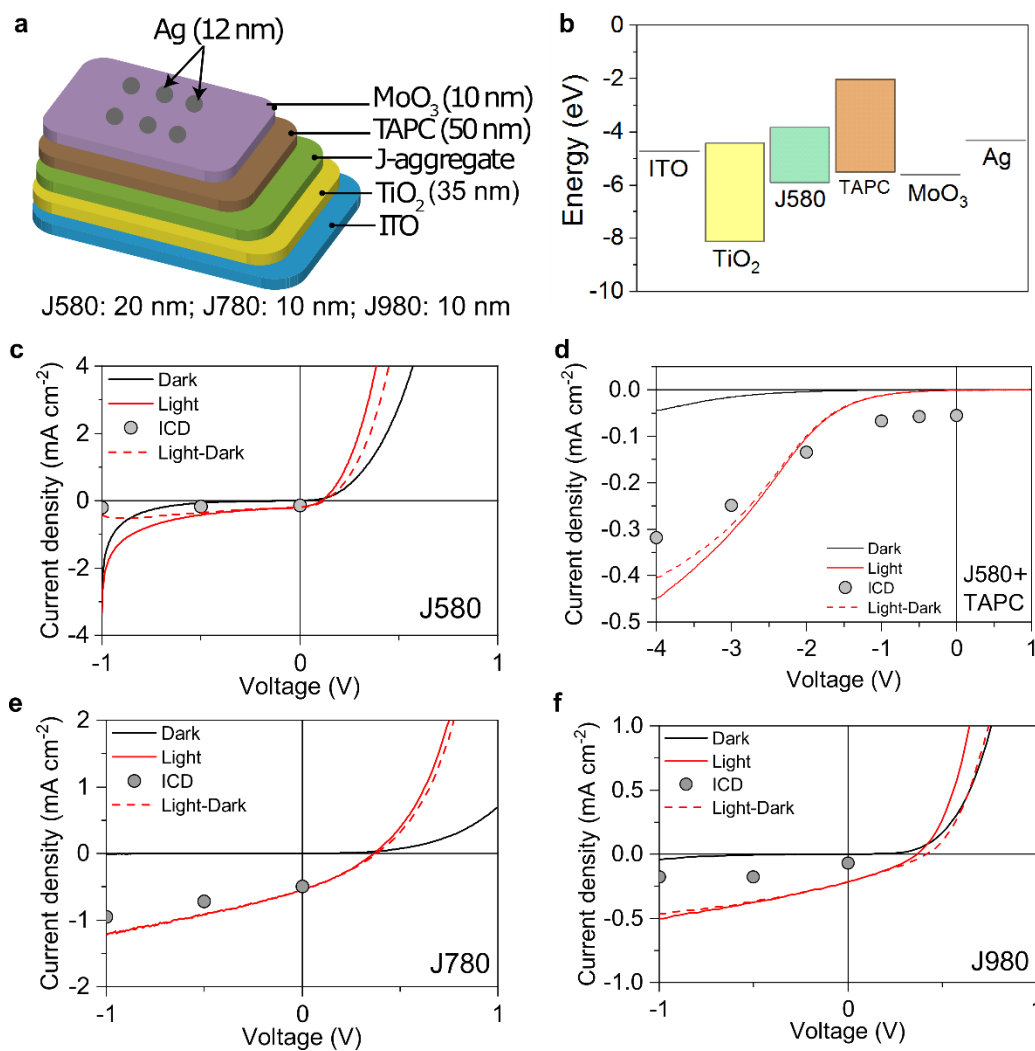


Fig. 3 (a) Device structure of narrowband photodetectors with J-aggregates as active layer. The active area is 3.1 mm². (b) Energy level diagram of the device for **J580** (optical gap) with TAPC layer. Current density – voltage characteristics for the **J580** (c), **J580** with TAPC layer (d), **J780** (e) and **J980** (f) devices measured under simulated solar light (red curves) and in the dark (black curves). The device structure was ITO/TiO₂/J-aggregate layer **J580** (20 nm), or **J580**+TAPC (50 nm) or **J780** (10 nm) or **J980** (10 nm)/MoO₃ (10 nm)/Ag (12 nm). The difference between the current-density curves under light and in the dark, respectively, is also indicated (dotted line). The integrated current density (ICD) values calculated from the external quantum efficiency are marked with circles.

peaks of the Xenon lamp in this spectral region. For **J580**+TAPC devices, the ICD even exceeds the J_{sc} value measured under simulated light. This is due to the sublinear J_{sc} response with increasing light intensity of these diodes. When calculating the ICD values from the EQE values measured at low light intensity, the non-linear response of the photodiode is not taken account of.

In summary, the smooth and continuous J-aggregate films obtained for in-situ deposition of **J780** and **J980** lead to a low dark current in reverse bias, which is favorable for light detection sensitivity. The significant improvement in the short circuit current-density for in-situ deposited films as compared to the J-aggregate films deposited by the direct method can be related to the particular morphology of the two films. While direct deposition leads to an assembly of two-dimensional J-aggregate platelets where a fraction of platelets are poorly connected to the TiO_2 surface, in-situ deposited films consist of a large fraction of small grains that are directly connected to the oxide surface allowing a more efficient exciton quenching by charge transfer. In the case of discontinuous J-aggregate morphologies, such as the ones observed for the **J580** devices deposited directly from solution, an additional electron blocking layer allows to reduce the dark current significantly.

The EQE was measured at different bias voltages using monochromatic light chopped at 85 Hz and is shown together with the calculated responsivities in Fig. 4 (a – d). The EQE closely follows the absorption spectrum for all the devices with similar FWHM values. Using the electron blocking layer (TAPC) in devices incorporating the **J580** dye allowed to increase the maximum EQE to 9.8% as compared to the maximum value of 7.8% reached in the absence of TAPC. This is due to better hole extraction in the presence of a strong electric field at high reverse bias.⁵⁵ In addition, the vapor deposited TAPC layer may also heal pinhole defects leading to the observed greatly reduced dark current. Furthermore, **J780** photodetectors show high EQE of 15% at -1 V reverse bias at 780 nm (Fig. 4c). The peak maximum and FWHM of

the EQE matches the absorption profile of **J780** (Fig. S7, ESI†), which is a significant achievement, given the fact that interference effects often introduce a mismatch between absorbance and EQE in complex device architectures.³⁹ Remarkably, **J980** based photodetectors allow to obtain considerably redshifted NIR photosensitivity at 980 nm with an EQE of 3.5 % at -1 V (Fig. 4d). An increased non-radiative relaxation channel of the exciton in the low bandgap aggregate (**J980**) competes with charge generation, which explains the moderate EQE.⁵⁶ Furthermore, the **J980** photodetector shows a small EQE response at 450 nm attributed to the S0-S2 transition.^{57,58} However, the EQE related to the S2 state is much lower than the one related to the S1 state unlike the strong response from the S2 state in quantum dot photodetectors.⁵⁹

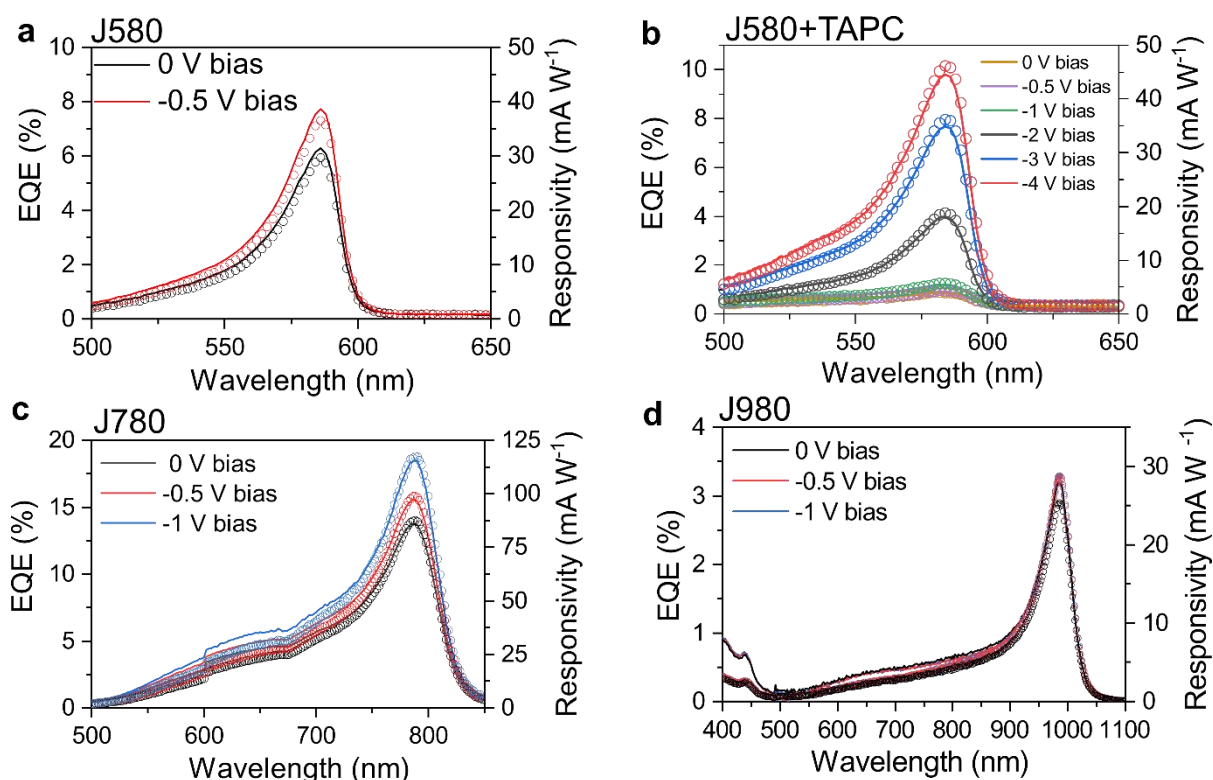


Fig. 4 External quantum efficiency (EQE) and responsivity (shown in open circles) of photodetectors showing wavelength-selectivity at 586 nm (without TAPC (a), with TAPC (b)),

at 780 nm (c) and at 980 nm (d) for **J580**, **J780** and **J980**, respectively, measured at an interval of 2 nm at different bias voltage.

Given the huge red-shift of the J-aggregate absorption band, the question arises whether electron injection from the exciton into the TiO₂ conduction band is still possible. One way to address this question is to start from the oxidation potential of J-aggregates which is lower by 0.2 to 0.8 V as compared to the HOMO level of the monomer.^{60,61} From here one can calculate the energy level from where electron injection occurs by adding the energy of the absorbed photon. In terms of electrochemical potentials this can be formally written as $\Phi(J^+/J^*) = \Phi(J^+/J_0) + h\nu$, where $\Phi(J^+/J_0)$ and $\Phi(J^+/J^*)$ are the oxidation potentials of the J-aggregate in its ground and excited state, respectively. Carrying out this calculation for the **J580** aggregate, we estimate the J-aggregate oxidation potential to be lower by 0.5 eV with respect to the monomer with oxidation potential at 1.86 V vs NHE,⁶¹ which gives $\Phi(J^+/J_0) = 1.36$ V vs NHE. Adding the photon energy at maximum absorption ($h\nu = 2.14$ eV) we arrive at $\Phi(J^+/J^*) = -0.78$ V vs NHE, which provides high enough driving force for electron injection into the TiO₂ conduction band at -0.5V vs NHE.⁶² Similar calculations could be carried out for the **J780** and **J980** aggregates but their redox potentials should be known. In analogy to related pentamethine and heptamethine dyes, we note that the oxidation potential decreases significantly with increasing chain length in the chromophore.⁶³ Also, a better estimation of the relative energy level positions should take account of interface dipole layers, which could well be present at the TiO₂ interface.

3.3. Current noise

Photodetector sensitivity is characterized by the normalized detectivity D^* , which is related to the noise equivalent power (NEP) by $NEP = (A\Delta f)^{1/2}/D^*$. The latter is derived from

the noise power spectral density (PSD) which is obtained from the noise current.⁴⁶ In organic materials based photodetectors, it was common practice to assume that shot noise (inferred from the dark current of the device) is the dominant source of noise. This approximation, however, turned out to be inappropriate and therefore a detailed noise analysis is necessary.^{64,65} Fig. 5 (a-d) shows the PSD measured for all four devices in the dark at various applied biases. At low frequencies, a typical $1/f^\alpha$ response prevails, with α close to unity. Generally the origin of the so-called flicker noise comes from the stochastic process of charge trapping and release⁶⁶ and increases with increasing dark current.⁶⁷ Clearly the **J580** based devices show the highest noise level while $1/f^\alpha$ noise is reduced in **J780** and **J980** devices by about two orders of magnitude. The difference between these devices is attributed to the strong variation in J-aggregate film morphology of the three dyes. Benefitting from the in-situ deposition approach, **J780** and **J980** films are smooth and continuous, while **J580** films formed by direct deposition are rough and present pinholes leading to high dark current in these devices. Strikingly the addition of a thin TAPC layer on top of the **J580** film greatly suppresses the noise current. For instance, comparing the noise power spectral density at 100 Hz for **J580** with and without the additional TAPC layer at a bias of -1 V shows a four order of magnitude difference in the $1/f^\alpha$ current noise (Fig. 5 a and b).

Interestingly, all spectra show a broadband, bias independent increase in noise PSD at higher frequencies, which becomes most visible for the devices with the lowest noise level (Fig. 5b). In order to assess the noise characteristics of the circuit in the absence of the photodiode stack, resistors were used in place of the photodiodes on the same test fixture. In the range of frequencies below the cut-off frequency of the circuit (typically $< 10^4$ Hz), a flat thermal noise is observed (Fig. S8, ESI[†]). However, the noise level is not independent of the resistance and increases with decreasing resistance. Impedance spectroscopy measurements of the three photodiodes **J580**+TAPC, **J780** and **J980** showed that the real part of the admittance also

increases with frequency following the same trend as the current noise (Fig. S9, ESI†). Since the thermal noise is proportional to the real part of the impedance,⁴⁶ the increase in PSD observed at higher frequencies is attributed to the increasing thermal noise. Eventually, noise values (S_n) at the -3dB frequency (as discussed below) were taken to calculate the NEP and specific detectivity as summarized in Table 1.

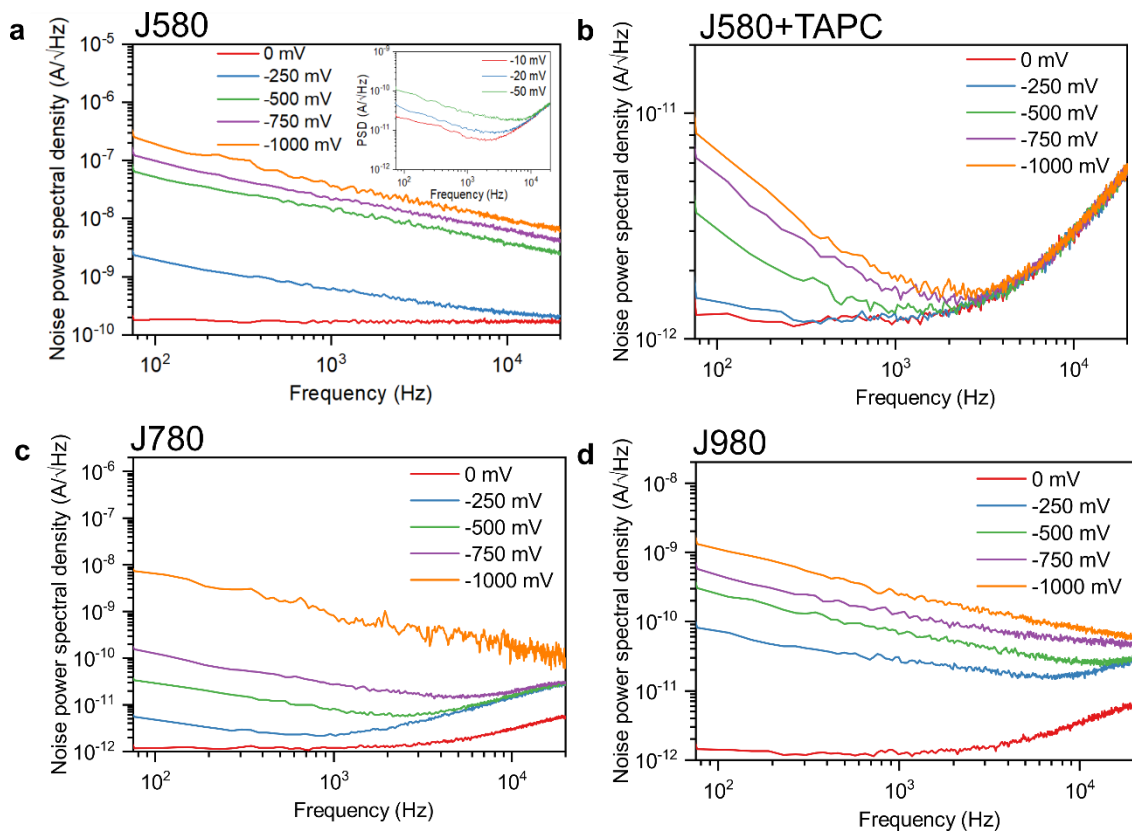


Fig. 5 Noise power spectral density plotted as a function of frequency for **J580** (a), **J580** with TAPC (b), **J780** (c) and **J980** (d) devices. The spectra were obtained at the indicated DC bias levels.

3.4. Response time and -3dB values

The response time of the detector was calculated from the rise time of the detector signal from 10 % to 90 % of the maximum photocurrent. A frequency modulated square wave light pulse

was used to determine the -3dB values (the power attenuation of -3dB corresponds to a current decrease by a factor of 0.707 with respect to the current value at saturation). An example of such a response time measurement is shown in Fig. 6a for the **J780** device. A similar trend in rise and decay current with bias voltage was observed for **J580** and **J980** devices. Generally, light can influence the resistance and capacitance of the device even at 0 V bias. With increasing light intensity, more excitons are created which leads to a higher charge carrier density. To evaluate this effect, we chose the **J580** device to measure the impedance at different light intensities (Fig. S10, ESI†). The increase in free charge carriers can decrease the resistance of the device, with a small increase in capacitance at low frequencies. A combined effect of resistance and capacitance influences the response time of the detector ($\tau_r = RC$). In our case, we concluded that the resistance of the device is the dominant factor determining response time, which can be strongly influenced by light intensity, considering the high photoconductive nature reported in cyanine devices when driven at high reverse bias.⁶⁸ For the -3dB measurement, the light intensity in our system was set such that J_{sc} corresponded to the current-density obtained under simulated AM1.5 solar irradiation and the bias voltage was varied from 0 V to -1 V.

To investigate the effects of light and bias voltage on the device, the device was preconditioned for 120 s at -1 V and a light intensity of 70%, followed by -3dB measurement at different bias voltage. The data plots for -3dB values for the devices measured with and without preconditioning are shown in the Supplementary Information (Fig. S11, ESI†) and summarized in Fig. 6b. The -3dB frequency slightly increases with bias voltage due to faster charge extraction, independent of the preconditioning. It can be noted that the **J980** device shows the fastest response time compared to the other photodetectors. Preconditioning the devices leads to a slight improvement in the response time as clearly evident in the **J780** devices. Nevertheless, the devices showed an upturn in the current attenuation in the low frequency

regime at higher bias voltage (Fig. S11, ESI†). This can be due to counterion migration in the active layer, which can form a space-charge layer, thereby influencing the response time of the detector.⁶⁹ The -3dB frequency values without pre-conditioning are summarized in Table 1 and were used to calculate NEP and specific detectivity D^* .

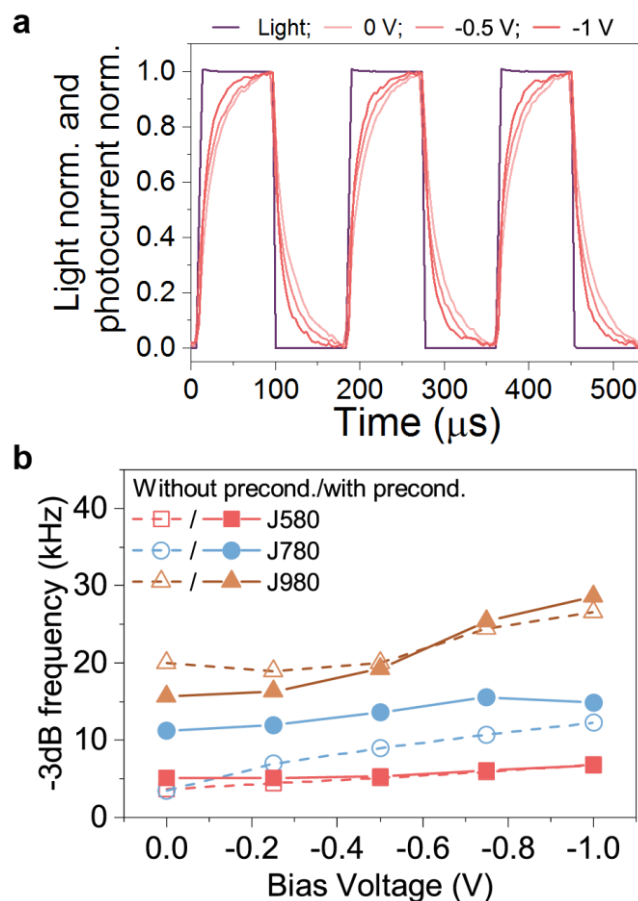


Fig. 6 Temporal response of the **J780** device illuminated with 10 kHz light pulses and measured at different bias voltage (a). Summary of -3dB values for all devices measured without and with pre-conditioning (b).

Table 1. Summary of figures of merit for solution processed narrowband photodetectors with FWHM of the EQE < 100 nm.

| Device (film thickness) | Strategy | Response peak (nm) | FWHM of the EQE (nm) | Bias (V) | Response speed, -3dB values (kHz) | EQE (%) | Responsivity (mA/W) | Noise power spectral density (S_n , A/ $\sqrt{\text{Hz}}$) @ -3dB value | Noise equivalent power (NEP, W/ $\sqrt{\text{Hz}}$) | Specific detectivity (D^* , Jones or $\text{cm}^2/\text{V}\sqrt{\text{Hz}}$) |
|---|--|--------------------|-------------------------|-------------------------|--------------------------------------|----------------------|---------------------|---|--|---|
| J580 (<10 nm) | This work – intrinsic absorption | 586 | 28 | 0 | 3.6 | 6.0 | 30 | $1.6 \cdot 10^{-10}$ | $5.5 \cdot 10^{-9}$ | $3.2 \cdot 10^7$ |
| | | | | -0.5 | 5.1 | 7.8 | 37 | $5.8 \cdot 10^{-9}$ | $1.6 \cdot 10^{-7}$ | $1.1 \cdot 10^6$ |
| J780 (<10 nm) | This work – intrinsic absorption | 780 | 72 | 0 | 3.5 | 14 | 87 | $1.6 \cdot 10^{-12}$ | $1.8 \cdot 10^{-11}$ | $9.7 \cdot 10^9$ |
| | | | | -0.5 | 9.0 | 16 | 99 | $1.5 \cdot 10^{-11}$ | $1.5 \cdot 10^{-10}$ | $1.2 \cdot 10^9$ |
| J980 (<10 nm) | This work – intrinsic absorption | 980 | 50 | 0 | 20 | 3.1 | 25 | $6.0 \cdot 10^{-12}$ | $2.4 \cdot 10^{-12}$ | $7.5 \cdot 10^8$ |
| | | | | -0.5 | 20 | 3.2 | 29 | $2.9 \cdot 10^{-11}$ | $1.0 \cdot 10^{-11}$ | $1.7 \cdot 10^8$ |
| Ketocyanines ⁵⁸ | Optical cavity | 525 | 90 | -1 | 20 | 17 | - | $4.50 \cdot 10^{-23}$ | $6.25 \cdot 10^{-24}$ | $1.00 \cdot 10^{10}$ |
| Merocyanine J-aggregate ⁶ | Intrinsic absorption | 747 | 30 | 0 | - | 9 | 55 | - | - | $9.00 \cdot 10^{10}$ |
| Cyanine J-aggregate (<10 nm) ³⁹ | Intrinsic absorption with optical cavity | 756 | 125 | 0 | 92 | 16.1 | 98 | - | - | $4.3 \cdot 10^{11}$ |
| Helical Nanoribbons (1 μm) ⁵⁹ | CCN | 575 | 22 | -3 | - | - | 8 | - | - | $2.60 \cdot 10^{10}$ |
| | | 600 | 19 | | - | - | 7.3 | - | - | $1.70 \cdot 10^{10}$ |
| | | 615 | 16 | | - | - | 3.4 | - | - | $1.10 \cdot 10^{10}$ |
| | | 645 | 20 | | - | - | 1.1 | - | - | $9.30 \cdot 10^9$ |
| P3HT:PCBM ($\sim \mu\text{m}$) ¹³ | Photo multiplication type | 650 | 29 | -10 | - | 49 | - | $3 \cdot 10^{-14}$ | $1.5 \cdot 10^{-12}$ | $1.30 \cdot 10^{11}$ |
| BODIPY sensitized Zn_{0.9}M_{0.1}O ⁶⁰ | Intrinsic absorption | 530 | 50 | 0.1 V/ μm | 0.001 | 1.87 $\cdot 10^4$ | 8 $\cdot 10^6$ | - | - | $1.70 \cdot 10^{12}$ |

“-” means not mentioned

3.5. Demonstration of inkjet printed narrowband photodetectors

We have selected the J-aggregate dye **J580** to study device fabrication by inkjet printing. Our main goal was to inkjet print the active J-aggregate film, but also to work towards an all-printed device. We therefore also inkjet printed the titania electron transporting layer.

The device was completed by vacuum deposition of the top layers in the device stack as shown in Fig. 7a. Generally, the solution used for spin-coating needs to be adapted for inkjet printing in order to produce homogeneous films. Good jetting is determined by the Weber and Reynolds numbers of the ink and defined in a stability window.^{70–72} Droplet formation can be followed by stroboscopy and has been optimized for the inks used here (Fig. S12, ESI†). Furthermore, the individual droplets need to merge to form a uniform layer upon solvent evaporation. Devices manufactured with the compact TiO₂ layer alone showed a very poor performance. A single printed layer was less than 10 nm thick and the film remained porous even after wet-on-wet printing of several layers. A non-homogeneous topography of the printed c-TiO₂ layer was imaged under AFM after annealing at 460 °C for 2 h (Fig. S13a, ESI†). This porosity may easily lead to a direct contact between ITO and vapor deposited MoO₃, given the fact that the J-aggregate layers in between are ultrathin and are not able to fill up all of the pinholes. As a consequence we observed lower EQE and lower $J_{\text{light}}/J_{\text{dark}}$ at comparable electric field. Our attempt to print several layers (up to 3 layers) of c-TiO₂ on top of each other resulted in disruption after sintering. To overcome this issue, we introduced a second, mesoporous TiO₂ layer (m-TiO₂) on top of the non-homogeneously covered c-TiO₂ layer. The m-TiO₂ layer (~100 nm thick) homogeneously covered the c-TiO₂ layer and ITO substrate (Fig. S13b, ESI†). Subsequently, the J-aggregates were printed on the m-TiO₂ layer. The *J-V* curves of the printed devices are shown in Figure. 7b. Upon addition of the m-TiO₂ layer, an enhancement in J_{sc} and V_{oc} as well as suppression of dark current was observed. This can be due to complete coverage of m-TiO₂ on the c-TiO₂ layer, which may lead to a reduction of shunts formed between ITO and J-aggregates. Additionally the increased performance may be related to improved charge extraction at the TiO₂/J-aggregate interface. As a result, the EQE of the J-aggregates printed on m-TiO₂ shows a 9-fold increase compared to the reference device (c-TiO₂ only) at -1 V (Fig. 7c and d). The introduction of a mesoporous layer is a well-known strategy used in dye

sensitized solar cells (DSSC) for enhancing charge extraction.^{70,72} Broadening the EQE in the presence of m-TiO₂ can be due to the increased adsorption of J-aggregates on mesoporous TiO₂, which can itself act as light scatterer. Secondly, the thick top electrode (60 nm) with buffer layers (TAPC and MoO₃) can introduce cavity effects where interference dominates the light absorption in the J-aggregate layer.³⁹ The response time of the inkjet printed device was also measured (Fig. 7e) and compared with the spin-coated **J580** device (Fig. 7f). As shown in section 2.3, the addition of a TAPC layer significantly decreased the current noise. However, a thick electron blocking (TAPC) layer increases the resistance for hole extraction and is known to reduce the response time of the photodetector.⁵⁴ Here, we have observed a significant improvement in the response time due to the presence of an increased interface area between the TiO₂/J-aggregate (upon addition of m-TiO₂ layer) leading to fast electron extraction, which speaks for overcoming the RC limit. To the authors' knowledge, this may be the first inkjet printed, truly ultra-narrowband photodetector with response speed (f_{3dB}) in the kHz range operating at low bias voltage (-1 V).

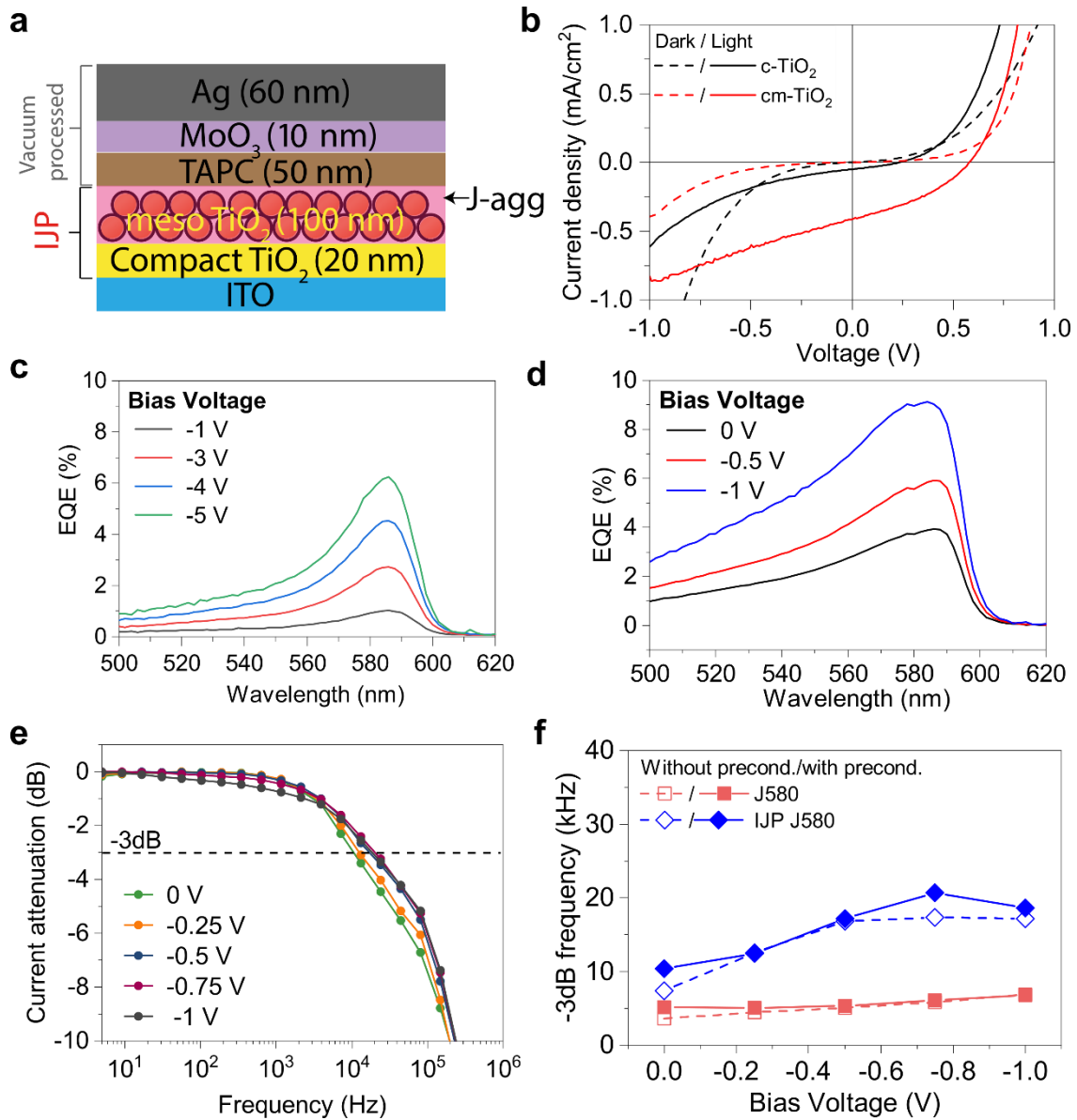


Fig. 7 Schematic of the device (cross-section) structure showing printed layers (c-TiO₂, m-TiO₂ and J-aggregate as active layer) followed by vacuum processed layers (a). Current density-voltage curves showing an increase in charge extraction upon addition of m-TiO₂ layer (b). EQE for inkjet printed device structure with J-aggregate as active layer on c-TiO₂ (c) and c-TiO₂/m-TiO₂ (d). -3dB value recorded for inkjet printed device (IJP J580) with c-TiO₂/m-TiO₂ at different bias voltage (e). -3dB values of the ink-jet printed device (diamonds) in comparison with a spin-coated device (squares) without m-TiO₂ layer (f).

4. Conclusion

Exploiting the intrinsic narrow absorption width and high extinction coefficient of J-aggregates, we were able to realize narrowband organic photodetectors with spectral bandwidth below 50 nm, while employing ultrathin active films of about 10-20 nm. Spectral sensitivity ranging from the red to the near infrared domain up to 1000 nm could be achieved by varying the polymethine length of the cyanine dyes. We explored different film forming approaches from solution and pinpointed the importance of balancing high quality J-aggregate assemblies and continuous thin film formation. To this aim, we demonstrated an in-situ growth method where J-aggregates were obtained as a thin film upon spin-coating monomer solutions. On the other hand, it was also possible to start from J-aggregate solutions, which can be processed into a thin continuous film. The latter method is particularly interesting for inkjet deposition. To underline scalable fabrication possibilities, we have demonstrated an inkjet printed device from aqueous solution showing similar performance to the spin-coated devices. We believe these findings will open new avenues for developing narrowband photodetectors and for scaling-up their fabrication.

Conflicts of Interest

There are no conflicts of interest to declare.

Acknowledgement

The authors gratefully acknowledge funding from the Swiss National Science Foundation under grant numbers: 200021-157135, IZRJZ2_164179/1 and 200021-169695, as well as from the Swiss Commission for Technology and Innovation (project perolec 18468.1 PFNM-NM). We acknowledge the Scanning Probe Microscopy user laboratory at Empa for providing access

to the instrument. We thank Anand Verma for extending his support with the inkjet printing. We acknowledge the use of the facilities of the Coating Competence Center at Empa.

References

- 1 H. Chen, K. Liu, L. Hu, A. A. Al-Ghamdi and X. Fang, *Mater. Today*, 2015.
- 2 M. Piels and J. E. Bowers, in *Photodetectors: Materials, Devices and Applications*, Woodhead Publishing, 2015, pp. 3–20.
- 3 M. Currie, in *Photodetectors: Materials, Devices and Applications*, Woodhead Publishing, 2015, pp. 121–155.
- 4 A. H. Atabaki, S. Moazeni, F. Pavanello, H. Gevorgyan, J. Notaros, L. Alloatti, M. T. Wade, C. Sun, S. A. Kruger, H. Meng, K. Al Qubaisi, I. Wang, B. Zhang, A. Khilo, C. V. Baiocco, M. A. Popović, V. M. Stojanović and R. J. Ram, *Nature*, 2018, **556**, 349–354.
- 5 C. L. Tan and H. Mohseni, *Nanophotonics*, 2018, **7**, 169–197.
- 6 A. Liess, A. Arjona-Esteban, A. Kudzus, J. Albert, A.-M. Krause, A. Lv, M. Stolte, K. Meerholz and F. Würthner, *Adv. Funct. Mater.*, 2019, **29**, 1805058.
- 7 Hamamatsu, S7505-01 RGB color sensor,
<https://www.hamamatsu.com/eu/en/product/type/S7505-01/index.html>.
- 8 R. Wang and F. Zhang, *J. Mater. Chem. B*, 2014, **2**, 2422.
- 9 R. Lukac, *J. Real-Time Image Process.*, 2006, **1**, 45–52.
- 10 K. Qiao, H. Deng, X. Yang, D. Dong, M. Li, L. Hu, H. Liu, H. Song and J. Tang, *Nanoscale*, 2016, **8**, 7137–7143.
- 11 Y. Fang, Q. Dong, Y. Shao, Y. Yuan and J. Huang, *Nat. Photonics*, 2015, **9**, 679.
- 12 Q. Lin, A. Armin, P. L. Burn and P. Meredith, *Nat. Photonics*, 2015, **9**, 687.

- 13 W. Wang, F. Zhang, M. Du, L. Li, M. Zhang, K. Wang, Y. Wang, B. Hu, Y. Fang and J. Huang, *Nano Lett.*, 2017, **17**, 1995–2002.
- 14 S. Yoon, K. M. Sim and D. S. Chung, *ACS Nano*, 2019, acsnano.8b08717.
- 15 B. Siegmund, A. Mischok, J. Benduhn, O. Zeika, S. Ullbrich, F. Nehm, M. Böhm, D. Spoltore, H. Fröb, C. Körner, K. Leo and K. Vandewal, *Nat. Commun.*, 2017, **8**, 15421.
- 16 A. Sobhani, M. W. Knight, Y. Wang, B. Zheng, N. S. King, L. V Brown, Z. Fang, P. Nordlander and N. J. Halas, *Nat. Commun.*, 2013, **4**, 1643.
- 17 X. Tang, G. fu Wu and K. W. C. Lai, *J. Mater. Chem. C*, 2017, **5**, 362–369.
- 18 K.-S. Cho, K. Heo, C.-W. Baik, J. Y. Choi, H. Jeong, S. Hwang and S. Y. Lee, *Nat. Commun.*, 2017, **8**, 840.
- 19 G. Konstantatos and E. H. Sargent, *Nat. Nanotechnol.*, 2010, **5**, 391–400.
- 20 J. R. Manders, T.-H. Lai, Y. An, W. Xu, J. Lee, D. Y. Kim, G. Bosman and F. So, *Adv. Funct. Mater.*, 2014, **24**, 7205–7210.
- 21 A. Solanki, S. Li, H. Park and K. B. Crozier, *ACS Photonics*, 2018, **5**, 520–527.
- 22 D. Yang and D. Ma, *Adv. Opt. Mater.*, 2019, **7**, 1800522.
- 23 W. Li, D. Li, G. Dong, L. Duan, J. Sun, D. Zhang and L. Wang, *Laser Photon. Rev.*, 2016, **10**, 473–480.
- 24 M. S. Bradley and V. Bulović, *Phys. Rev. B*, 2010, **82**, 33305.
- 25 J. R. Tischler, M. S. Bradley, V. Bulović, J. H. Song and A. Nurmikko, *Phys. Rev. Lett.*, 2005, **95**, 36401.
- 26 A. C. Véron, H. Zhang, A. Linden, F. Nüesch, J. Heier, R. Hany and T. Geiger, *Org. Lett.*, 2014, **16**, 1044–1047.
- 27 H. Zhang, S. Jenatsch, J. De Jonghe, F. Nüesch, R. Steim, A. C. Véron and R. Hany, *Sci. Rep.*, 2015, **5**, 9439.

- 28 T. Geiger, H. Benmansour, B. Fan, R. Hany and F. Nüesch, *Macromol. Rapid Commun.*, 2008, **29**, 651–658.
- 29 M. Bates and R. R. Lunt, *Sustain. Energy Fuels*, 2017, **1**, 955–968.
- 30 T. Tani, in *J-aggregates*, World Scientific, 1996, pp. 209–228.
- 31 R. S. Eachus, A. P. Marchetti and A. A. Muentner, *Annu. Rev. Phys. Chem.*, 1999, **50**, 117–144.
- 32 M. Shakiba, K. K. Ng, E. Huynh, H. Chan, D. M. Charron, J. Chen, N. Muhanna, F. S. Foster, B. C. Wilson and G. Zheng, *Nanoscale*, 2016, **8**, 12618–12625.
- 33 N. A. Leclaire, M. Li, A. C. Véron, A. Neels, J. Heier, J. R. Reimers and F. A. Nüesch, *Phys. Chem. Chem. Phys.*, 2018, **20**, 29166–29173.
- 34 E. E. Jelley, *Nature*, 1937, **139**, 631.
- 35 T. Kobayashi, *J-Aggregates*, World Scientific, 1996.
- 36 F. Würthner, T. E. Kaiser and C. R. Saha-Möller, *Angew. Chemie Int. Ed.*, 2011, **50**, 3376–3410.
- 37 T. E. Kaiser, H. Wang, V. Stepanenko and F. Würthner, *Angew. Chemie*, 2007, **119**, 5637–5640.
- 38 S. B. Anantharaman, D. Messmer, A. Sadeghpour, S. Salentinig, F. Nüesch and J. Heier, *Nanoscale*, 2019, **11**, 6929–6938.
- 39 T. P. Osedach, A. Iacchetti, R. R. Lunt, T. L. Andrew, P. R. Brown, G. M. Akselrod and V. Bulović, *Appl. Phys. Lett.*, 2012, **101**, 113303.
- 40 H. Shekhar, V. Lami, O. Solomeshch, A. Fenigstein, L. Tomer, L. Becky, Y. Vaynzof and N. Tessler, *Org. Electron.*, 2019, **67**, 1–9.
- 41 F. P. de Arquer, A. Armin, P. Meredith and E. H. Sargent, *Nat. Rev. Mater.*, 2017, **2**, 16100.
- 42 G. Pace, A. Grimoldi, M. Sampietro, D. Natali and M. Caironi, *Semicond. Sci.*

- Technol.*, 2015, **30**, 104006.
- 43 Y. Yu, I. Hajime, Y. Kenichi, K. Noriyuki, W. Hirofumi, M. Masaya and O. Yuji, *Jpn. J. Appl. Phys.*, 2010, **49**, 10204.
 - 44 Y. Yang, S. Omi, R. Goto, M. Yahiro, M. Era, H. Watanabe and Y. Oki, *Org. Electron.*, 2011, **12**, 405–410.
 - 45 M. J. Alam and D. C. Cameron, *J. Sol-Gel Sci. Technol.*, 2002, **25**, 137–145.
 - 46 S. Kogan, *Electronic noise and fluctuations in solids*, Cambridge University Press, 1996.
 - 47 M. S. Bradley, J. R. Tischler and V. Bulović, *Adv. Mater.*, 2005, **17**, 1881–1886.
 - 48 S. B. Anantharaman, T. Stöferle, F. A. Nüesch, R. F. Mahrt and J. Heier, *Adv. Funct. Mater.*, 2019, **29**, 1806997.
 - 49 H. v Berlepsch and C. Böttcher, *Phys. Chem. Chem. Phys.*, 2018, **20**, 18969–18977.
 - 50 S. B. Anantharaman, EPFL, 2019.
 - 51 M. S. Bradley, J. R. Tischler and V. Bulović, *Adv. Mater.*, 2005, **17**, 2147.
 - 52 H. Aviv and Y. R. Tischler, *J. Lumin.*, 2015, **158**, 376–383.
 - 53 C.-H. Cheng, Z. Li, A. Hambarde and P. B. Deotare, *ACS Appl. Mater. Interfaces*, 2018, **10**, 39336–39342.
 - 54 J. Li, Y. Zheng, D. Zheng and J. Yu, *J. Photonics Energy*, 2016, **6**, 35502.
 - 55 J. W. Lee, D. Y. Kim and F. So, *Adv. Funct. Mater.*, 2015, **25**, 1233–1238.
 - 56 R. Englman and J. Jortner, *Mol. Phys.*, 1970, **18**, 145–164.
 - 57 P.-A. Bouit, C. Aronica, L. Toupet, B. Le Guennic, C. Andraud and O. Maury, *J. Am. Chem. Soc.*, 2010, **132**, 4328–4335.
 - 58 C. Villegas, E. Krokos, P.-A. Bouit, J. L. Delgado, D. M. Guldi and N. Martín, *Energy Environ. Sci.*, 2011, **4**, 679–684.
 - 59 J. W. Lee, D. Y. Kim, S. Baek, H. Yu and F. So, *Small*, 2016, **12**, 1328–1333.

- 60 M. Kawasaki and T. Sato, *J. Phys. Chem. B*, 2000, **105**, 796–803.
- 61 J. L. Lyon, D. M. Eisele, S. Kirstein, J. P. Rabe, D. A. VandenBout and K. J. Stevenson, *J. Phys. Chem. C*, 2008, **112**, 1260–1268.
- 62 M. Grätzel, *Inorg. Chem.*, 2005, **44**, 6841–6851.
- 63 R. O. Loutfy, J. H. Sharp, *Photogr. Sci. Eng.*, 1976, **20**, 165.
- 64 Y. Yao, Y. Liang, V. Shrotriya, S. Xiao, L. Yu and Y. Yang, *Adv. Mater.*, 2007, **19**, 3979–3983.
- 65 I. K. Kim, J. H. Jo, J. B. Lee and Y. J. Choi, *Org. Electron.*, 2018, **57**, 89–92.
- 66 M. Bag, N. S. Vidhyadhiraja and K. S. Narayan, *Appl. Phys. Lett.*, 2012, **101**, 43903.
- 67 G. Konstantatos, I. Howard, A. Fischer, S. Hoogland, J. Clifford, E. Klem, L. Levina and E. H. Sargent, *Nature*, 2006, **442**, 180–183.
- 68 L. Wang, S. Jenatsch, B. Ruhstaller, C. Hinderling, D. Gesevičius, R. Hany and F. Nüesch, *Adv. Funct. Mater.*, 2018, **28**, 1705724.
- 69 S. Jenatsch, L. Wang, N. Leclaire, E. Hack, R. Steim, S. B. Anantharaman, J. Heier, B. Ruhstaller, L. Penninck, F. Nüesch and others, *Org. Electron.*, 2017, **48**, 77–84.
- 70 S. G. Hashmi, M. Özkan, J. Halme, S. M. Zakeeruddin, J. Paltakari, M. Grätzel and P. D. Lund, *Energy Environ. Sci.*, 2016, **9**, 2453–2462.
- 71 Y. Oh, H. G. Yoon, S.-N. Lee, H.-K. Kim and J. Kim, *J. Electrochem. Soc.*, 2011, **159**, B34--B38.
- 72 R. Cherrington, D. J. Hughes, S. Senthilarasu and V. Goodship, *Energy Technol.*, 2015, **3**, 866–870.